1-1-2019

Yolk-Shell Structured FeP@C Nanoboxes as Advanced Anode Materials for Rechargeable Lithium-/Potassium-Ion Batteries

Fuhua Yang
University of Wollongong, fy896@uowmail.edu.au

Hong Gao
University of Wollongong, hg173@uowmail.edu.au

Junnan Hao
University of Wollongong, jh845@uowmail.edu.au

Shilin Zhang
University of Wollongong, sz384@uowmail.edu.au

Peng Li
University of Wollongong, pl465@uowmail.edu.au

See next page for additional authors

Yolk-Shell Structured FeP@C Nanoboxes as Advanced Anode Materials for Rechargeable Lithium-/Potassium-Ion Batteries

Abstract

Maintaining structural stability and alleviating the intrinsic poor conductivity of conversion-type reaction anode materials are of great importance for practical application. Introducing void space and a highly conductive host to accommodate the volume changes and enhance the conductivity would be a smart design to achieve robust construction; effective electron and ion transportation, thus, lead to prolonged cycling life and excellent rate performance. Herein, uniform yolk-shell FeP@C nanoboxes (FeP@CNBs) with the inner FeP nanoparticles completely protected by a thin and self-supported carbon shell are synthesized through a phosphidation process with yolk-shell Fe_2O_3@CNBs as a precursor. The volumetric variation of the inner FeP nanoparticles during cycling is alleviated, and the FeP nanoparticles can expand without deforming the carbon shell, thanks to the internal void space of the unique yolk-shell structure, thus preserving the electrode microstructure. Furthermore, the presence of the highly conductive carbon shell enhances the conductivity of the whole electrode. Benefiting from the unique design of the yolk-shell structure, the FeP@CNBs manifests remarkable lithium/potassium storage performance.

Disciplines

Engineering | Physical Sciences and Mathematics

Publication Details

Authors

Fuhua Yang, Hong Gao, Junnan Hao, Shilin Zhang, Peng Li, Yuqing Liu, Jun Chen, and Zaiping Guo

Yolk-shell structured FeP@C nanoboxes as advanced anode materials for rechargeable lithium/potassium ion batteries

Fuhua Yang [a], Hong Gao [a], Junnan Hao [a], Shilin Zhang [a], Peng Li [a], Yuqing Liu [b], Jun Chen [b] [*], Zaiping Guo [a] [*]

[a] Institute for Superconducting and Electronic Materials, School of Mechanical, Materials and Mechatronics Engineering, University of Wollongong, North Wollongong, NSW 2500, Australia. E-mail: zguo@uow.edu.au

[b] ARC Centre of Excellence for Electromaterials Science, Intelligent Polymer Research Institute, Australian Institute of Innovative Materials, University of Wollongong, North Wollongong, NSW 2522, Australia. E-mail: junc@uow.edu.au

Abstract

Maintaining structural stability and alleviating the intrinsic poor conductivity of conversion-type reaction anode materials are of great importance for practical application. Introducing void space and a highly conductive host to accommodate the volume changes and enhance the conductivity would be a smart design to achieve robust construction, effective electron and ion transportation, thus, lead to prolonged cycling life, and excellent rate performance. Herein, uniform yolk-shell FeP@C nanoboxes (FeP@CNBs) with the inner FeP nanoparticles completely protected by a thin and self-supported carbon shell were synthesized through a phosphidation process with yolk-shell Fe_2O_3@CNBs as precursor. The volumetric variation of the inner FeP nanoparticles during cycling is alleviated and the FeP nanoparticles can expand without deforming the carbon shell, thanks to the internal void space of the unique yolk-shell

structure, thus preserving the electrode microstructure. Furthermore, the presence of the highly conductive carbon shell enhances the conductivity of the whole electrode. Benefiting from the unique design of the yolk-shell structure, the FeP@CNBs manifests remarkable lithium/potassium storage performance. The as-prepared FeP@CNBs electrode exhibits a high capacity of 609 mAh g^{-1} at 100 mA g^{-1} and excellent cycling stability without any significant capacity loss in lithium-ion batteries (476 mAh g^{-1} after 400 cycles at 500 mA g^{-1}). In the case of potassium-ion batteries, a reversible capacity of 205 mAh g^{-1} was retained after 300 cycles at 100 mA g^{-1}.

1. Introduction

Because of their high energy and power densities, lithium ion batteries (LIBs) have been extensively investigated and widely as the power for portable electronics and electrical vehicles[1][2][3]. For large-scale stationary energy storage, however, such as electrical grids, the limited and uneven distribution of lithium resources in the Earth's crust is restricting the further development of LIBs[1][4]. Recently, potassium ion batteries (PIBs) have attracted tremendous attention as a potential alternative to LIBs, due to the abundant potassium reserves on Earth and its low standard hydrogen potential (-2.93 V versus E^o), close to that of lithium (-3.04 V versus E^o)[5][6]. The large potassium ion radius (1.38 Å) results in sluggish kinetics, however, during electrochemical processes[5][7]. Although unremitting efforts have been devoted to and great progress achieved in the development of energy storage materials, there is still a long way to go to achieve feasible anode materials for LIBs and PIBs with satisfactory capacity. Among the various proposed anode materials, including carbonaceous materials[8][9],

alloy materials[10][11], metal phosphides[12][13], and metal sulphides[14][15], iron phosphide

is one of the most appealing anode materials for both LIBs and PIBs, because of the

abundance of its raw materials (Fe and P) and its high theoretical capacity of ~926 mAh

g^{-1}[16]. Nevertheless, FeP undergoes large volume expansion (~200 %) during the

lithiation/potassiation process, leading to pulverization of the electrode materials and

fast capacity fading during long-term cycling[17]. What is more, the relatively low

electronic conductivity of FeP affects the electrochemical redox reactions to some

extent and leads to low utilization of the active materials[18]. To address these issues,

FeP with various nanostructures have been proposed, and tuning the morphology and

structure has been proven to be an effective way to address the above

challenges.[19][20][21][22][23][16] Nanostructured FeP can not only reduce the electron and

ions transport paths, but also buffers the strain resulting from volume expansion[18]. For

instance, FeP/C nanocubes that consist of FeP nanoparticles distributed in a carbon

scaffold have been fabricated[21]. The carbon matrix enhances the conductivity of the

electrode and enables fast electron/ion transportation. The unique structure provides

abundant reactive sites that are evenly distributed in the carbon nanocubes. As a result,

improved electrochemical performance is achieved. Similarly, carbon-coated FeP

nanoplates were reported, in which the two-dimensional (2D) nanostructure releases

the mechanical strain and buffers the drastic volume expansion to achieve stable cycling

performance[20]. Even though improvement of the electrochemical performance has

been achieved by introducing conductive carboneous materials into FeP, the structural

integrity of the electrode during the cycling process is still a challenge that needs to be

addressed. Therefore, developing a novel FeP based hybrid by introducing particles with a void space and an integrated carbon shell to control the volume changes, shorten the electron/ion diffusion paths, and improve the whole conductivity could be a potential strategy to further promote its electrochemical performance.

Herein, yolk-shell structured FeP@carbon nanoboxes (FeP@CNBs) have been synthesized through a novel phosphidation-in-nanobox strategy. By confining FeP particles in hollow carbon cubes, this unique architectural design offers multiple advantages for addressing the problems associated with FeP during electrochemical processes. The complete and robust carbon shell can not only facilitate efficient electron transfer and enhance the electrical conductivity of the composite, but also prevents the agglomeration of the active materials. More importantly, the extra void space of the yolk-shell structure can accommodate the large volume variation of FeP and maintain the integrity of the electrode microstructure. Furthermore, the nanoboxes are expected to have higher tap density than other nanostructures, which is a significant parameter for electrode materials with high volumetric energy density. The as-synthesized FeP@CNBs electrode has demonstrated a high reversible capacity of 609 and 205 mAh g^{-1} at 100 mA g^{-1} for LIBs and PIBs, respectively. Remarkable rate performance (380 mAh g^{-1} at 2 A g^{-1}) and ultra-long cycling life (476 mAh g^{-1} after 400 cycles at 500 mA g^{-}) in LIBs have also been achieved.

2. Experimental section

2.1.Material synthesis

Synthesis of Fe_2O_3 nanocubes: Fe_2O_3 nanocubes were prepared using the hydrothermal

4

method[24]. In the typical synthesis process, 16.22 g $FeCl_3$ was added into 50 mL

deionized water to produce a brown solution. Then, 50 mL of 5.4 M NaOH solution

was added into the brown solution under magnetic stirring at 75 °C. The resultant

solution was then transferred to an autoclave, which was kept at 100 °C for 4 days. After

the autoclave was cooled down to room temperature, the product was harvested by

centrifugation and washed several times in de-ionized water. The resultant composite

was then dried in a 70 °C vacuum oven for 12 h.

Synthesis of Fe_2O_3@polydopamine (PDA) core-shell nanocubes[25]: 400 mg as-

prepared Fe_2O_3 nanocubes were first dispersed into 500 mL of 10 mM Tris-buffer

solution by ultrasonication for 30 min. Then, 200 mg of dopamine hydrochloride was

added into the above solution, which was kept stirring for 10 hours. The resultant

product was collected via centrifugation and washed three times with deionized water

and ethanol, respectively, and dried at 70 °C overnight.

Synthesis of yolk-shell Fe_2O_3@CNBs[26]: the as-prepared core-shell Fe_2O_3@PDA

nanocubes were annealed at 550 °C for 2 h in Ar with a heating rate of 3 °C min^{-1} to

yield the core-shell Fe_2O_3@C nanocubes. Then, the as-obtained core-shell Fe_2O_3@C

nanocubes was dispersed in 4 M HCl solution with stable stirring for 1 h to partially

etch the Fe_2O_3 core to yield the yolk-shell Fe_2O_3@C nanoboxes. After rinsing,

centrifugation, and drying at 70 °C overnight, the yolk-shell Fe_2O_3@C was harvested.

The carbon nanoboxes were prepared by increasing the etching time to 12 h.

Synthesis of yolk-shell FeP@CNBs[27]: Yolk-shell FeP@CNBs were synthesized in a

two-zone furnace. Typically, 1 g NaH_2PO_2 was loaded into an alumina boat which was

put at the center of the upstream zone, while another alumina boat containing 50 mg

yolk-shell Fe_2O_3@C was put in the center of the downstream zone. Flowing Ar gas was

initially passed through the tube for 2 h to remove the air. Subsequently, the temperature

of the upstream zone was raised to 300 ^oC and held for 1.5 h with a heating rate of 2 ^oC

min^{-1}, meanwhile, the temperature of the downstream zone was raised to 550 ^oC and

held for 2 h with a heating rate of 5 ^oC min^{-1}. After the furnace was cooled down, the

yolk-shell FeP@C nanoboxes were obtained. For comparison, FeP nanocubes were

synthesized by using the Fe_2O_3 nanocubes as the precursor, The phosphidation process

was the same to that for yolk-shell FeP@C nanoboxes.

2.2.Materials characterization:

The crystal structures of the as-obtained material were measured using X-ray diffraction

(XRD, GBC MMA diffractometer, Cu Kα lines, λ = 1.54056 Å) with a scanning rate of

1° min^{-1}. Raman spectra were collected on a JobinYvon HR800 Raman spectrometer.

X-ray photoelectron spectroscopy (XPS) experiments were carried out using a VG

multilab 2000 (VG Inc.), and all the binding energy data were calibrated using the C 1s

peak at 284.8 eV of the surface adventitious carbon. The photoelectron spectrometer

used monochromatic Al Kα radiation under vacuum of 2 × 10^{-6} Pa. The morphology

and particle sizes of the as-synthesized samples were characterized on a JEOL JSM-

7500FA field-emission scanning electron microscope (FESEM). The details of the

crystal structure and EDS mapping were further examined by scanning transmission

electron microscope (STEM, JEOL JEM-ARM200F), which was conducted at 200 kV.

Thermogravimetric analysis (TGA; TA Instruments 2000) was conducted under air

from 25 to 700°C with a heating rate of 5 °C min^{-1}.

2.3. Electrochemical measurements

The working electrodes were prepared by a slurry-coating method. Typically, the prepared materials were ground carefully with Super P and carboxymethyl cellulose (CMC) in a weight ratio of 8:1:1 in deionized water to form a slurry. Then, the as-prepared slurry was spread out on copper foil using a doctor blade, and the foil was dried at 80 °C under vacuum conditions overnight. The electrochemical tests were conducted with CR 2032 coin type cells, which were assembled in an argon-filled glove box. In the lithium ion batteries (LIBs), the counter electrode was a disk of lithium metal, and Celgard 2400 were used as separator. The electrolyte was 1 M $LiPF_6$ in ethylene carbonate (EC)/diethyl carbonate (DEC)/dimethyl carbonate (DMC) (1:1:1 by volume). In the case of the potassium ion batteries (PIBs), the electrolyte consisted of a solution of 0.8 M KPF_6 in ethylene carbonate (EC)/diethyl carbonate (DEC) (1:1 by volume). The counter and reference electrodes were potassium metal, and the separator was glass fiber. Cyclic voltammetry was carried out on a VMP-3 electrochemical workstation at a scan rate of 0.1 mV s^{-1}. The charge-discharge tests were conducted on a Land CT2001A battery tester over the voltage range of 0.01-2.5V at different constant current densities. All the specific capacities were based on the weight of the composites. If no special

2.4. Hydrogen evolution reaction characterization and performance test

All electrochemical characterization and performance tests were carried out in a three-electrode configuration in an electrolyte of 0.5 M H_2SO_4 solution on a VMP3 Biologic

potentiostat. The counter and reference electrodes were platinum wire and Ag/AgCl in

saturated KCl electrode, respectively. To prepare the working electrodes, 4 mg active

materials was first added into 1 mL of a solution consisting of a 9:1 (v/v) ratio of

absolute ethanol to Nafion (5 wt%). Then, the as-prepared suspension was sonicated

for 2 h to produce a homogeneous ink. After that, 10 μl of the ink was then drop-casted

onto a glassy carbon electrode as working electrode. Linear sweep voltammetry (LSV)

was conducted with a scan rate of 5 mV s^{-1}. Electrochemical impedance spectroscopy

(EIS) was performed in frequencies ranging from 100 kHz to 0.1 Hz. Potentials were

converted from Ag/AgCl to reversible hydrogen electrode (RHE) via $+ (0.197 + 0.0592$

pH) V.

3. Results and discussion

Figure 1a illustrates the detailed synthesis procedure for the FeP@CNBs, which

consists of hydrothermal reaction, carbon-coating, Fe_2O_3 etching, and the

phosphidation process. First, monodisperse Fe_2O_3 nanocubes were facilely synthesized

by hydrothermal reaction and used as the starting materials. Subsequently, a layer of

carbon was uniformly and firmly coated on the surfaces of the Fe_2O_3 nanocubes by

polydopamine-coating and a high temperature annealing treatment[28]. As shown in

Figure 1b and c, the as-synthesized Fe_2O_3@C nanocubes maintain the morphology of

the Fe_2O_3 nanocube precursor with a smooth carbon shell. The thickness of the carbon

layer was around 30 nm, which can be identified from the TEM image (Figure 1c). In

order to form the yolk-shell structure, core-shell Fe_2O_3@C nanocubes were dispersed

into hydrochloric acid solution (HCl) for Fe_2O_3 etching. In this step, the Fe_2O_3 core was

partially removed, and a void space between the Fe_2O_3 and the carbon shell was formed

(Figure 1d and e). It is notable that the void space can be controlled by the HCl etching

time. When the etching time was extended to 12 h, the Fe_2O_3 core was totally removed,

and the hollow carbon nanocubes were harvested (Figure S1). The above yolk-shell

Fe_2O_3@C nanoboxes were then subjected to a phosphidation process, during which the

Fe_2O_3 yolk was chemically transformed to FeP, and thus, uniform yolk-shell

FeP@CNBs were obtained (Figure 1 f and g). As shown in the XRD patterns (Figure

1h), during the synthesis process for the FeP@CNBs, the starting materials, α-Fe_2O_3

nanocubes, with correspondingly indexed XRD patterns (JCPDS 33-0664), were

transformed to γ-Fe_2O_3@C nanocubes (JCPDS 33-0664) after the high temperature

annealing. All the XRD peaks of the FeP@CNBs can be indexed to orthorhombic FeP

(JCPDS: 89-2746) without any obvious impurities, indicating that the γ-Fe_2O_3

nanoparticles inside the carbon nanoboxes were successfully transformed to pure-phase

FeP crystals during the phosphidation process. Similarly, FeP nanocubes were also

synthesized thought the same phosphidation procedure, except that α-Fe_2O_3 nanocubes

were used as the precursors (Figure S2). All the XRD peaks of the FeP nanocubes

obtained from the phosphidation of α-Fe_2O_3 nanocubes also can be indexed to

orthorhombic FeP (JCPDS: 89-2746) (Figure S3).

The scanning electron microscope (SEM) images of the FeP@CNBs (Figure 2a and b),

show that the as-obtained FeP@CNBs were highly uniform with an average particle

size of ~400 nm, consistent with the Fe_2O_3@CNBs precursor. The yolk-shell structure

is confirmed in the TEM images (Figure 2d and e). In the high-resolution TEM

(HRTEM) image (Figure 2c), the lattice of (200) and (103) crystal planes with a *d*-spacing of 0.256 and 0.182 nm, respectively, is observed. Alongside the magnified TEM image, the fast Fourier transform (FFT) pattern is consistent with the XRD result. Furthermore, the energy-dispersive X-ray spectroscopy (EDX) elemental mapping results (Figure 2f, g, h, and i) show that the distribution of Fe and P is concentrated around the central cores, verifying the existence of the FeP cores in the carbon nanoboxes. The yolk-shell structure is believed to be important for the electrochemical performance of the composite. With the advantages of FeP cores to deliver high reversible capacity, the carbon shell to improve the electronic conductivity of the composite, and void space to accommodate the volume variation, satisfactory electrochemical performance of the FeP@CNBs can be anticipated. Further evidence for the formation of the FeP@CNBs was obtained from the X-ray photoelectron spectroscopy (XPS) analysis (Figure 2k, l, and m). The XPS survey scan spectrum revealed the presence of Fe, P, C, and O on the surface of the FeP@CNBs. In the high-resolution Fe 2p XPS spectrum, two peaks with binding energy of 711.2 and 724.5 eV were observed, which can be assigned to the Fe $2p_{3/2}$ and Fe $2p_{1/2}$ peaks, respectively[29]. In the high resolution P 2p XPS spectrum, the two peaks centered at 129.3 and 130.2 eV corresponded to the binding energy of P $2p_{3/2}$ and P $2p_{1/2}$, respectively[16]. Furthermore, the peak located at 133.6 eV is attributed to PO_4^{3-} or P_2O_5, which is caused by the oxidation of P species because of contact with air[30][31]. In the Raman spectra the intensity ratios of the D to the G band (I_D/I_G) for the FeP@CNBs and γ-Fe_2O_3@C nanocubes were calculated to be 0.90 (Figure S5), suggesting the presence of a

disordered and amorphous carbon component in both composites, which would be favorable to improve the diffusion rate of Li^+/K^+ ions and electrons[32]. In order to determine the FeP content of the FeP@CNBs, thermal analysis was performed on the FeP nanocubes and FeP@CNBs (Figure S4). In the case of FeP@CNBs, a weight increase was observed between 450-600 °C in the TGA curve, which was due to the oxidation of FeP to Fe_2O_3 and P_2O_5 in the air[23]. In the case of the FeP@CNBs, a small weight loss of about 2 wt% first occurred below 100 °C because of the removal of adsorbed water on the surface of the FeP@CNBs. After that, another weight loss took place between 420-500 °C before the weight increased between 500-600 °C. It is believe that both carbon burning and FeP oxidation occurred between the 420-600 °C. The carbon burning was the dominant process between 420-500 °C, however, and thus, a weight loss was observed. Whereas, the FeP oxidation caused the weight increase from 500 to 600 °C. Based on the TGA results forFeP@CNBs and FeP nanocubes, the weight contents of FeP and carbon were calculated to be 81wt% and 19wt%, respectively.

The lithium storage behavior of the FeP@CNBs was first investigated by cyclic voltammetry (CV) at a scan rate of 0.1 mV s^{-1} in the voltage range of 0.01-2.5 V. Figure 3a shows the representative CV curves from the first to the fourth cycles. In the first cathodic scan, two cathodic peaks located at 1.2 and 1.0 V are observed. The 1.2V peak can be explained by the intercalation of Li^+ into the FeP to form Li_xFeP (FeP + xLi^+ + $xe^- \rightarrow LixFeP$ ($x = 0$-3))[33]. Whereas, the 1.0 V peak is associated with the formation of solid-electrolyte interphase (SEI) film and the reduction of Li_xFeP to Fe and Li_3P (Li_xFeP + (3-x)Li^+ + (3-x)$e^- \rightarrow$ Fe + Li_3P)[34]. During the following anodic scan, only

11

1   one broad peak centered at 1.1 V was observed, which is related to the oxidation of Fe

2   to FeP. It is noteworthy that there is an obvious difference between the first and the

3   following cycles, that is, the cathodic peak shifted to 0.6 V after the first cycle.

4   Nevertheless, both the cathodic and anodic peaks in the CV curves overlap from the

5   second cycle onward, suggesting the excellent reversibility and stability of the electrode.

6   A similar phenomenon is also observed in the CV curves of the FeP nanocubes (Figure

7   S6).

8   The lithium storage performance was also investigated by galvanostatic discharge-

9   charge measurements. The FeP@CNBs delivered a high discharge capacity of 1125.5

10   mAh g^{-1} and a charge capacity of 762.8 mAh g^{-1} in the first cycle, giving an initial

11   coulombic efficiency of 67.8%. The 32.2 % irreversible capacity loss of the initial cycle

12   can be attributed to the formation of the SEI layer on the surface of the FeP@CNBs and

13   electrolyte decomposition. Unexpectedly, as shown in the charge-discharge profile

14   (Figure 2b), there were no obvious plateaus, but sloping lines are observed at 0.6 and

15   1.1 V in discharge and charge curves, respectively, which can be explained by

16   insufficiently active reactions in the lithiation of FeP to Li$_x$FeP (x = 0-3) and the reverse

17   delithiation of Li$_x$FeP (x = 0-3) to FeP[16][32]. Figure 3c presents the cycling performance

18   of the FeP@CNBs at a current density of 100 mAh g^{-1}. As expected, the FeP@CNBs

19   electrode manages to maintain a high reversible capacity of 609 mAh g^{-1} after 70 cycles

20   without any distinct decay, indicating remarkable cycling stability. Based on the content

21   of FeP (81%) in the FeP@CNBs and the reversible capacity (250 mAh g^{-1}) contributed

22   by the carbon hollow spheres (Figure S8), the utilization rate of the FeP was calculated

to be 75%. In contrast, the FeP nanocubes show a relatively low reversible capacity of

477.5 mAh g^{-1} in the first cycle, and it decreases to 250 mAh g^{-1} after 70 cycles at 100

mA g^{-1}. To further evaluate the cycling stability of the FeP@CNBs, a long-term cycling

test was conducted. The results show that the FeP@CNBs achieved a high initial

reversible capacity of 545 mAh g^{-1} and retained a charge capacity of 476 mAh g^{-1} after

400 cycles at 500 mAh g^{-1} (Figure 3e). Apart from its remarkable cycling performance,

FeP@CNBs demonstrated excellent rate capability at varied current rates. As shown in

Figure 3d, FeP@CNBs delivered high specific capacities of 608, 563, 490, 441, and

380 mAh g^{-1} at 0.1, 0.2, 0.5, 1, and 2 A g^{-1}, respectively, which is much higher than for

the FeP nanocubes, revealing the excellent kinetics of the FeP@CNBs. The effects of

the yolk-shell structure towards improving the lithium storage performance of the

composite were further investigated by the EIS analysis comparing the FeP@CNBs and

FeP nanocubes electrodes (Figure 3f). The results show that the interfacial resistance of

the FeP@CNBs is smaller than that of the FeP nanocubes electrode, which can be

explained by the presence of the highly conductive carbon shell[16]. Furthermore, the

morphology of the FeP@CNBs electrode after 70 cycles at 100 mA g^{-1} was

characterized by TEM (Figure 3g). It is clear that the yolk-shell structure of the

FeP@CNBs was retained, with a layer of SEI also present on the surface of the carbon

shell. Void space can still observed in the TEM image, indicating that the void space in

the FeP@CNBs is large enough to accommodate the volume changes during the

repeated charge-discharge processes. *Ex situ* XRD was also performed to identify the

composition of the FeP@CNBs (Figure S 9). Cells were disassembled after charged in

the 70th cycle to 2.5V and the working electrodes were washed with propylene carbonate to remove the residual $LiPF_6$, the XRD patterns of the cycled working electrode consist of FeP and Cu signals due to the use of Cu as current collector. Apart from the Cu and FeP peaks, no other peaks are observed in the XRD results, indicating that the composition of the working electrode turned back to FeP after 70 cycles in Lithium ion batteries.

Potassium storage properties were also examined. In the CV curves of both the FeP@CNBs (Figure 4a) and the FeP nanocubes (Figure S10) electrodes, only two peaks located at 0.8 and 2.0 V were observed in the cathodic and anodic scans after the first cycle, respectively, associated with the potassiation and de potassiation of FeP. The profiles of the charge-discharge curves are consistent with the CV results, with sloping plateaus at 0.8 and 2.0 V appearing in the discharge and charge curves, respectively (Figure 4b). Similar to the LIBs voltage profiles, the voltage profiles of KIBs are also sloping and no obvious plateaus observed, which can be ascribed to the insufficient activity of the potassiation/depotassiation reactions. The cycling performance of the FeP@CNBs at 100 mA g^{-1} within a voltage range of 0.01-2.5 V is shown in Figure 4c. Similar to the LIB performance, the PIBs exhibited high reversible capacity of 264 mAh g^{-1} in the first cycle with an initial coulombic efficiency of 47% and remarkable cycling stability. The loss the first reversible capacities is mainly ascribed to the decomposition of electrolyte to form a surface passivation SEI layer. Apart from this, another reason is that inreversible K ion trapped into the porous structure of the carbon layer and lattice of the FeP.[35,36] TEM is performed to identify the morphology and structure of the

FeP@CNBs after the first potassiation. It is clearly that yolk-shell structure is maintained after the first potassiation (Figure S 11). No obvious capacity loss was observed over 300 cycles and a capacity as high as 205 mA g^{-1} was obtained. Considering that the reversible capacity contributed from the carbon hollow spheres is negligible after 50 cycles (Figure S12), most of the reversible capacity must have come from the active materials. In order to confirm the importance of the yolk-shell structure for the electrochemical performance, the cycling performance of FeP nanocubes were evaluated for comparison under the same conditions. The FeP nanocubes, however, only offered a low reversible capacity of 189 mA g^{-1} in the first cycle and showed gradual capacity fading in the subsequent cycles. The relatively low reversible capacity of the FeP nanocubes is abscribed to low utilization of the bare FeP nanocubes resulting from the relatively low conductivity of the FeP.

Figure 4d shows the rate capacity performances of both FeP@CNBs and FeP nanocubes under different current densities ranging from 0.1 to 2 A g^{-1}. In the case of the FeP@CNBs, reversible capacities of 201, 156, 101, 65 and 37 mAh g^{-1} are obtained at 0.1, 0.2, 0.5, 1 and 2 A g^{-1}, respectively. Furthermore, the capacity of the FeP@CNBs could be restored back to 200 mAh g^{-1} when the current density was set back to 0.1 A g^{-1}, indicating the outstanding potassium storage performance of FeP@CNBs. Comparisons between our work and the state-of-the-art results reported for previous research on FeP based anode materials are also provided in Table S1. The cycling and rate performances of FeP@CNBs in LIBs are comparable to those for most reported anodes. The remarkable electrochemical performance of the FeP@CNBs can be

ascribed to the advantages of the yolk-shell structure. First, the carbon shell, which

serves as a self-supporting framework, can prevent the aggregation of FeP particles.

This carbon shell is well maintained even when the FeP expands during the

lithiation/potassiation processes, thanks to the sufficient void space of the yolk-shell

structure. What is more, the growth of a stable SEI layer on the surface of the carbon

shell, in turn, prevents the continual rupturing and reformation of the SEI, which occurs

commonly in all alloy-based anode materials. Second, the highly electronically and

ionically conducting carbon shell greatly enhances the transport kinetics. Third, the

electrode microstructure can be well preserved due to the void space, which allows the

FeP to expand without deforming the electrode microstructure, so that pulverization is

prevented. It is also notable that FeP@CNBs has also been demonstrated as a promising

option for the hydrogen evolution reaction (Figure S13), due to its advantages.

4. Conclusions

In summary, yolk-shell structured FeP carbon nanoboxes (FeP@CNBs) consisting of

FeP nanoparticles surrounded and protected by a carbon shell, have been developed and

proved to be a promising materials for rechargeable batteries and the hydrogen

evolution reaction. Benefiting from its unique structural features, the FeP@CNBs

electrode achieved remarkable electrochemical performance. Notably, the existence of

the carbon shell can prevent the aggregation of the FeP nanoparticles and enhance the

conductivity of the composite, while the void space between the carbon shell and the

FeP accommodates the volume expansion of the FeP during charge-discharge without

destroying the electrode microstructure. As a result, the FeP@CNBs electrode has

16

achieved high reversible capacity, superior rate performance, and an extremely stable cycling life.

References:

[1]   J. M. Tarascon, M. Armand, *Nature* **2001**, *414*, 359.

[2]   M. Armand, J.-M. Tarascon, *Nature* **2008**, *451*, 652.

[3]   X. Xu, W. Liu, Y. Kim, J. Cho, *Nano Today* **2014**, *9*, 604.

[4]   J. B. Goodenough, K. S. Park, *J. Am. Chem. Soc.* **2013**, *135*, 1167.

[5]   W. Zhang, W. K. Pang, V. Sencadas, Z. Guo, *Joule* **2018**, *2*, 1534.

[6]   A. Eftekhari, Z. Jian, X. Ji, *ACS Appl. Mater. Interfaces* **2016**, *9*, 4404.

[7]   H. Gao, T. Zhou, Y. Zheng, Q. Zhang, Y. Liu, J. Chen, H. Liu, Z. Guo, *Adv. Funct. Mater.* **2017**, *27*, 1702634.

[8]   S. Jin, J. Li, C. Daniel, D. Mohanty, S. Nagpure, D. L. Wood, *Carbon* **2016**, *105*, 52.

[9]   B. Cao, Q. Zhang, H. Liu, B. Xu, S. Zhang, T. Zhou, J. Mao, *Adv. Energy Mater.* **2018**, *8, 1801149.*

[10] Y. Liu, Z. Tai, T. Zhou, V. Sencadas, J. Zhang, L. Zhang, K. Konstantinov, Z. Guo, H. K. Liu, *Adv. Mater.* **2017**, *29*, 1703028.

[11] I. Sultana, T. Ramireddy, M. M. Rahman, Y. Chen, A. M. Glushenkov, *Chem. Commun.* **2016**, *52*, 9279.

[12] W. Zhang, J. Mao, S. Li, Z. Chen, Z. Guo, *J. Am. Chem. Soc.* **2017**, *139*, 3316.

[13] C. Wu, P. Kopold, P. A. van Aken, J. Maier, Y. Yu, *Adv. Mater.* **2017**, *29*, 1.

[14] S. H. Choi, Y. C. Kang, *Small* **2014**, *10*, 474.

[15] Y. Liu, Z. Tai, J. Zhang, W. K. Pang, Q. Zhang, H. Feng, K. Konstantinov, Z. Guo, H. K. Liu, *Nat. Commun.* **2018**, *9*, 3645.

[16] X. Wang, K. Chen, G. Wang, X. Liu, H. Wang, *ACS Nano* **2017**, *11*, 11602.

[17] M. Walter, M. I. Bodnarchuk, K. V. Kravchyk, M. V. Kovalenko, *Chim. Int. J. Chem.* **2015**, *69*, 724.

[18] F. Yang, H. Gao, J. Chen, Z. Guo, *Small Methods* **2017**, *1*, 1700216.

[19] F. Han, C. Y. J. Tan, Z. Gao, *ChemElectroChem* **2016**, *3*, 1054.

[20] F. Han, C. Zhang, J. Yang, G. Ma, K. He, X. Li, *J. Mater. Chem. A* **2016**, *4*, 12781.

[21] Y. Von Lim, S. Huang, Y. Zhang, D. Kong, Y. Wang, L. Guo, J. Zhang, Y. Shi, T. P. Chen, L. K. Ang, H. Y. Yang, *Energy Storage Mater.* **2018**, *15*, 98.

[22] M. Pramanik, Y. Tsujimoto, V. Malgras, S. X. Dou, J. H. Kim, Y. Yamauchi,

Chem. Mater. **2015**, *27*, 1082.

[23] J. Jiang, C. Wang, J. Liang, J. Zuo, Q. Yang, *Dalt. Trans.* **2015**, *44*, 10297.

[24] X. Y. Yu, L. Yu, L. Shen, X. Song, H. Chen, X. W. Lou, *Adv. Funct. Mater.* **2014**, *24*, 7440.

[25] F. Yang, Z. Zhang, K. Du, X. Zhao, W. Chen, Y. Lai, J. Li, *Carbon* **2015**, *91*, 88.

[26] X. Yu, H. Hu, Y. Wang, H. Chen, X. W. D. Lou, *Angew. Chemie Int. Ed.* **2015**, *54*, 7395.

[27] N. K. A. Venugopal, S. Yin, Y. Li, H. Xue, Y. Xu, X. Li, H. Wang, L. Wang, *Chem. - An Asian J.* **2018**, *13*, 679.

[28] Y. Liu, K. Ai, L. Lu, *Chem. Rev.* **2014**, *114*, 5057.

[29] G. Yunle, G. Fan, Q. Yitai, Z. Huagui, Y. Ziping, *Mater. Res. Bull.* **2002**, *37*, 1101.

[30] P. Jiang, Q. Liu, Y. Liang, J. Tian, A. M. Asiri, X. Sun, *Angew. Chemie Int. Ed.* **2014**, *53*, 12855.

[31] R. Wu, D. P. Wang, K. Zhou, N. Srikanth, J. Wei, Z. Chen, *J. Mater. Chem. A* **2016**, *4*, 13742.

[32] B. Wang, W. Al Abdulla, D. Wang, X. S. Zhao, *Energy Environ. Sci.* **2015**, *8*, 869.

[33] S. Boyanov, J. Bernardi, F. Gillot, L. Dupont, M. Womes, J.-M. Tarascon, L. Monconduit, M.-L. Doublet, *Chem. Mater.* **2006**, *18*, 3531.

[34] F. Han, L. Ma, Q. Sun, C. Lei, A. Lu, *Nano Res.* **2014**, *7*, 1706.

[35] X. Hu, Y. Jin, B. Zhu, Y. Tan, S. Zhang, L. Zong, Z. Lu, J. Zhu, *ChemNanoMat* **2016**, 2, 671.

[36] X. Yang, C. Wang, Y. Yang, Y. Zhang, X. Jia, J. Chen, X. Ji, *J. Mater. Chem. A*

1   **2016**, 3, 8800.

2

3

4
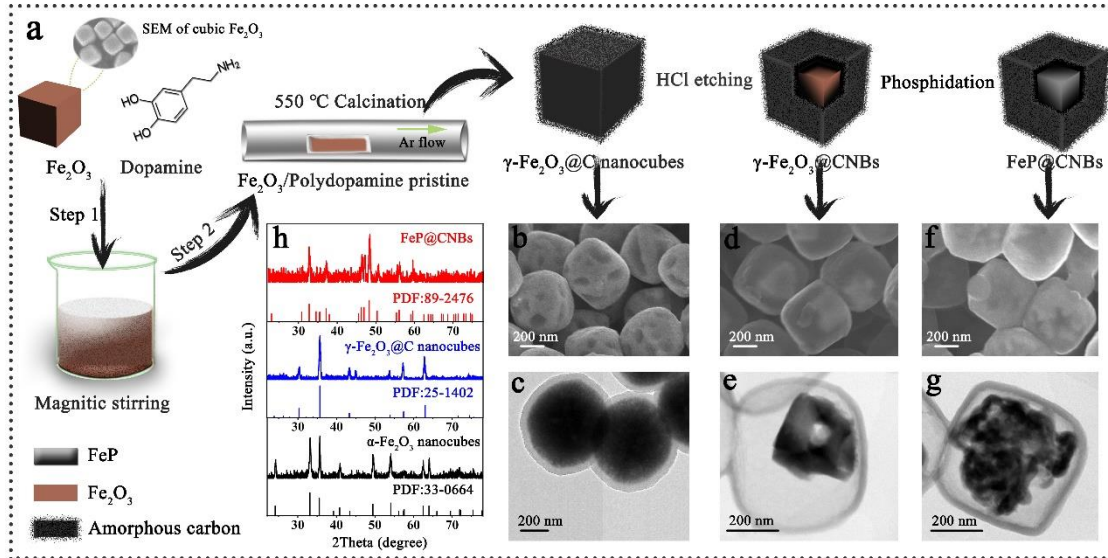
Figure 1. Schematic illustration of the yolk-shell structured FeP@C nanobox design and characterization of the intermediate materials

(a) Schematic illustration of the synthesis process for the FeP@CNBs; (b, d, and f) SEM and (c, e, and g) TEM images of Fe_2O_3@C nanocubes (b and c), Fe_2O_3@CNBs (d and e), and FeP@CNBs (f and g); (h) XRD patterns of the intermediate materials.

10

11

12

13
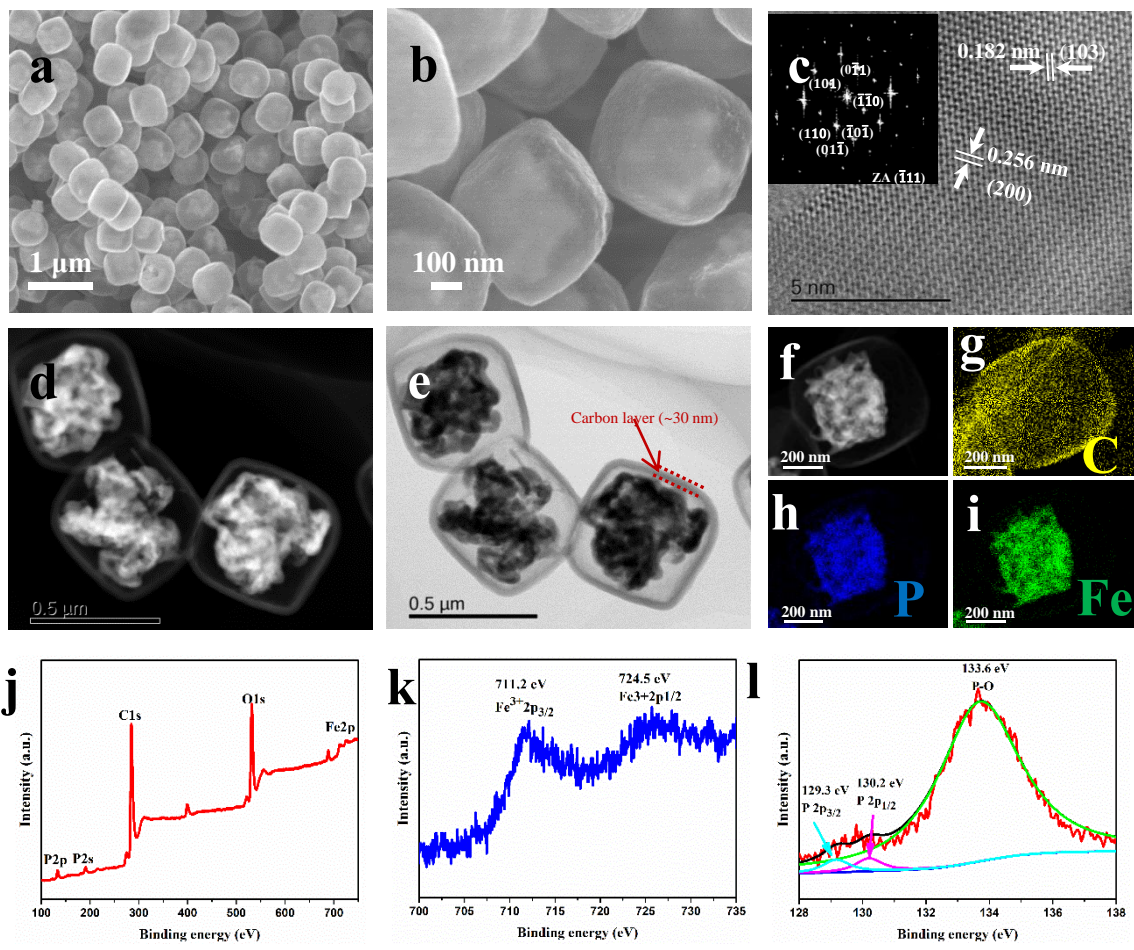
Figure 2. Characterization of the FeP@CNBs

(a and b) SEM images, (c) HRTEM image with the corresponding FFT pattern in the inset, (d) dark-field and (e) bright-field TEM images, and (f, g, h, and i) elemental mapping analysis of FeP@CNBs; (j, k and l) XPS spectra of FeP@CNBs: survey spectrum (k), Fe 2p (l), and P 2p (m).
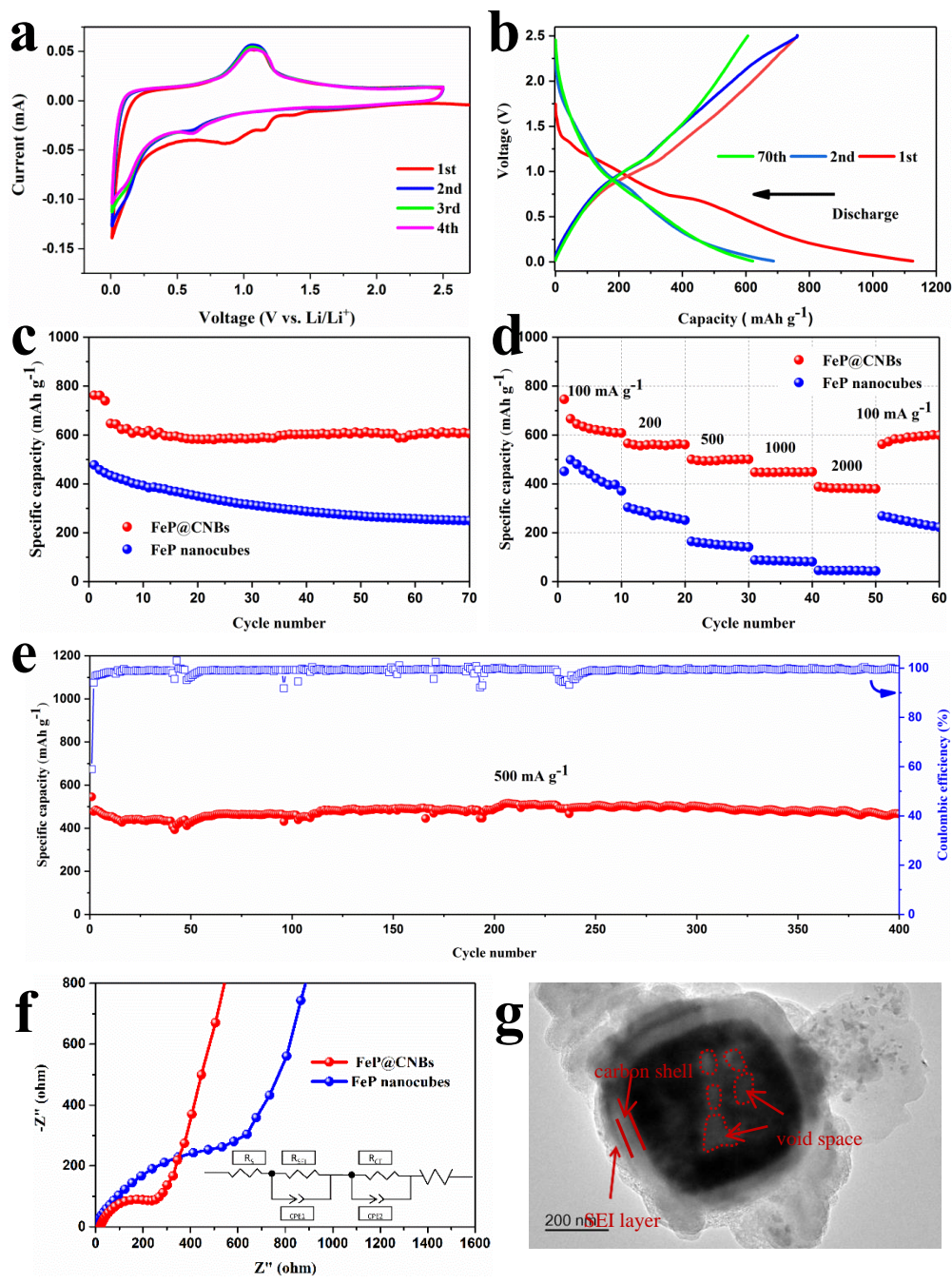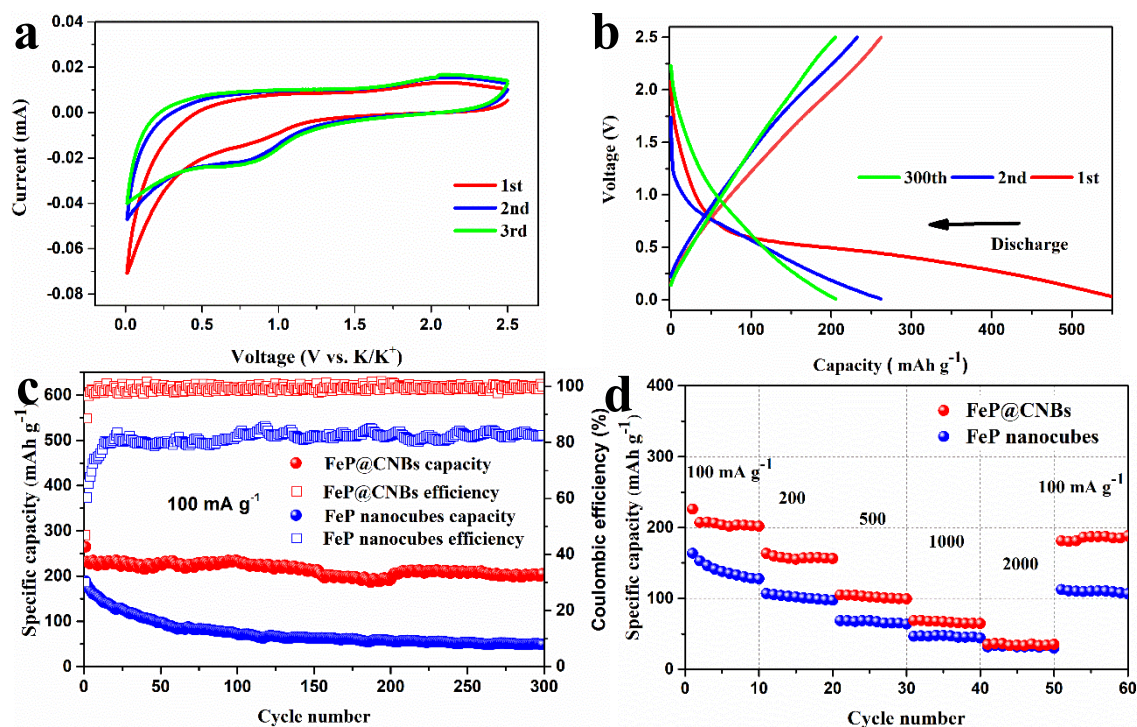
Figure 3. Lithium storage properties of FeP@CNBs.

(a) CV curves of the FeP@CNBs in the first four cycles. (b) Charge/discharge curves of FeP@CNBs electrode at 0.1 A g^{-1} in the 1st, 2nd, and 70th cycles. (c) Cycling performance of the FeP@CNBs and the FeP nanocubes at 0.1 A g^{-1}. (d) Rate performance of the FeP@CNBs and FeP nanocube electrodes at varied current densities. (e) Long-term cycling of the FeP@CNBs electrode at 500 mA g^{-1}. (f) Nyquist plots of the FeP@CNBs and FeP nanocubes, with the inset showing the equivalent circuit. (g) TEM image of FeP@CNBs after 70 cycles at 0.1 A g^{-1}. The capacities here are charge

22

Figure 4. Potassium storage properties of FeP@CNBs.

(a) CV curves of the FeP@CNBs in the first four cycles. (b) Charge/discharge curves of FeP@CNBs electrode at 0.1 A g^{-1} in the 1st, 2nd, and 300th cycles. (c) Cycling performance of FeP@CNBs and FeP nanocubes at 0.1 A g^{-1}. (d) Rate performance of the FeP@CNBs and the FeP nanocubes electrodes at varied current densities. The capacities here are charge capacity.

Table of content:

A unique yolk-shell structured FeP@C nanobox is developed as effective nanostructured anode materials for rechargeable batteries. The complete and robust carbon shell can not only facilitate efficient electron transfer and enhance the electrical conductivity of the composite, but also prevents the agglomeration of the active materials. More importantly, the extra void space of the yolk-shell structure can accommodate the large volume variation of FeP and maintain the integrity of the electrode microstructure. Thus, high reversible capacity and long cycling life are achieved in lithium/potassium ion batteries.

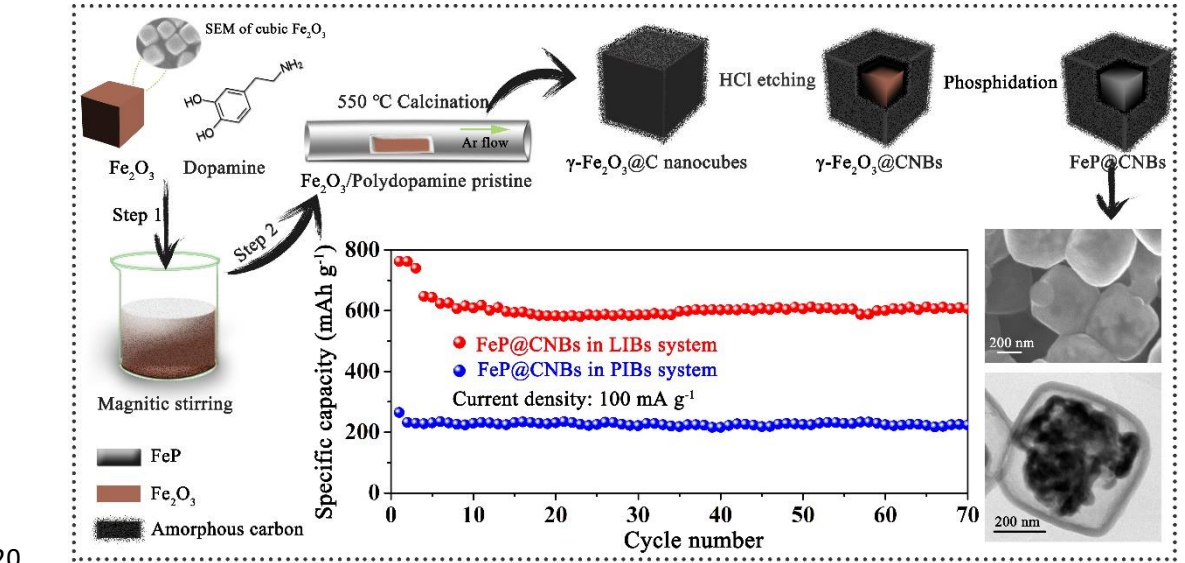**Authors**: Fuhua Yang [a], Hong Gao [a], Junnan Hao [a], Shilin Zhang [a], Peng Li [a], Yuqing Liu [b], Jun Chen [b*], Zaiping Guo [a*]

Title: Yolk-shell structured FeP@C nanoboxes as advanced anode materials for rechargeable lithium/potassium ion batteries